

# Renormalizable Spectral-Shell Dynamics as the Origin of Neural Scaling Laws

Yizhou Zhang<sup>\*1</sup>

<sup>1</sup>zyizhou96@gmail.com

## Abstract

Neural scaling laws and double-descent phenomena suggest that deep-network training obeys a simple macroscopic structure despite highly nonlinear optimization dynamics. We derive such structure directly from gradient descent in function space. For mean-squared error loss, the training error evolves as  $\dot{e}_t = -M(t)e_t$  with  $M(t) = J_{\theta(t)}J_{\theta(t)}^*$ , a time-dependent self-adjoint operator induced by the network Jacobian. Using Kato perturbation theory, we obtain an exact system of coupled modewise ODEs in the instantaneous eigenbasis of  $M(t)$ .

To extract macroscopic behavior, we introduce a logarithmic spectral-shell coarse-graining and track quadratic error energy across shells. Microscopic interactions within each shell cancel identically at the energy level, so shell energies evolve only through dissipation and external inter-shell interactions. We formalize this via a *renormalizable shell-dynamics* assumption, under which cumulative microscopic effects reduce to a controlled net flux across shell boundaries. This shell-form equation unifies lazy-regime training and feature learning as two limits of the same spectral-shell dynamics.

Assuming an effective power-law spectral transport in a relevant resolution range, the shell dynamics admits a self-similar solution with a moving resolution frontier and explicit scaling exponents, which explains neural scaling laws and double descent.

## 1 Introduction

Modern deep neural networks are trained by strongly nonlinear and high-dimensional optimization procedures. Nevertheless, across architectures, datasets, and training recipes, their performance exhibits remarkably simple and robust regularities.

---

<sup>\*</sup>Corresponding Author

Most prominently, empirical studies have shown that training and test losses obey approximate power laws in model size, dataset size, or total compute over wide dynamic ranges [Hestness et al., 2017, Kaplan et al., 2020, Henighan et al., 2020, Hoffmann et al., 2022, Hernandez et al., 2021, Wei et al., 2022]. Related law-like behaviors have been observed in precision scaling, pruning, sparsification, and model densification [Kumar et al., 2024, Sorscher et al., 2022, Rosenfeld et al., 2021, Blalock et al., 2020, Xiao et al., 2025]. These phenomena strongly suggest the existence of an underlying macroscopic structure governing how error is redistributed and dissipated during training.

**Limitations of existing theories.** A classical theoretical explanation is provided by the neural tangent kernel (NTK) framework [Jacot et al., 2018b, Lee et al., 2019a, Bietti and Bach, 2021], which models training as a linear dynamics in function space with a fixed kernel. While this perspective explains certain spectral biases and convergence rates, it relies on a frozen feature map and breaks down once representation learning becomes significant. Recent work has therefore emphasized feature-learning dynamics, using mean-field, tensor-program, or dynamical systems approaches [Yang, 2021, Canatar and Pehlevan, 2022, Bordelon et al., 2024, Bordelon and Pehlevan, 2024, Wang et al., 2023]. These models successfully capture richer behavior beyond the lazy regime, but typically treat NTK-like and feature-learning regimes via distinct approximations and do not provide a single operator-level equation that interpolates continuously between them.

**A spectral-shell perspective.** In this work, we take a function-space and operator-theoretic viewpoint. For mean-squared error loss, the training error  $e_t$  evolves according to the exact linear equation

$$\dot{e}_t = -M(t)e_t, \quad M(t) = J_{\theta(t)}J_{\theta(t)}^*,$$

where  $M(t)$  is a time-dependent, self-adjoint operator induced by the network Jacobian. Rather than assuming fixed features or a prescribed kernel, we analyze the training dynamics directly through the evolving spectral structure of  $M(t)$ .

Using Kato perturbation theory, we derive an exact system of coupled mode-wise ODEs in the instantaneous eigenbasis of  $M(t)$ . The resulting dynamics are fully rigorous but highly nonlocal across modes. To extract macroscopic behavior, we introduce a logarithmic *spectral-shell coarse-graining* and track the evolution of *quadratic error energy* within each shell. A key structural fact is that microscopic interactions within a shell, arising from eigenbasis drift, are strictly anti-symmetric and cancel identically at the level of quadratic energy. Consequently, shell energies evolve only through dissipation and *external interaction effects*—namely, energy exchange with other shells.

**Renormalizable shell dynamics.** This observation leads to an exact shell-level energy balance law. To close it at macroscopic scales, we introduce a *renormalizable shell-dynamics assumption*: after coarse-graining, the cumulative effect of microscopic degrees of freedom can be absorbed into a controlled net flux across shell boundaries, with subleading corrections becoming negligible. This notion of renormalizability is inspired by analogous constructions in statistical physics and condensed-matter theory, and it does not require a continuum limit nor impose any *a priori* direction of spectral transport.

When spectral shells are sufficiently dense over a dynamically relevant range, the shell dynamics admits a continuum approximation in the spectral variable  $\lambda$ , yielding an effective transport–dissipation equation. We emphasize that this PDE is a convenient representation of shell dynamics, not its fundamental starting point. Throughout the paper, renormalizability and effective power-law transport are treated as macroscopic assumptions, not as consequences of weak coupling or locality.

**Effective transport and scaling laws.** We further assume that, in the relevant resolution range, the renormalized spectral flux can be summarized by an effective power-law transport form. Under this single coarse-grained assumption, the shell dynamics admits a self-similar solution with a moving resolution frontier, geometric amplitude growth, and power-law dissipation. This structure yields explicit scaling-law exponents and provides a unified explanation for neural scaling laws and double-descent phenomena.

Within this framework, lazy (NTK-like) training and feature learning arise as two limits of the same spectral-shell dynamics. When the effective transport vanishes, the dynamics reduce to pure dissipation with fixed features. When transport is active, spectral mass flows across resolutions, inducing representation learning. Thus, both regimes—and the continuum between them—are unified by a single operator-level shell dynamics governing the redistribution of error during training.

## 2 Preliminaries: Function-Space Dynamics and Error Evolution

We consider supervised learning with mean-squared error (MSE) loss in the Hilbert space  $H = L^2(p)$  induced by the data distribution  $p(x)$ . All functions are identified up to sets of measure zero, and the inner product is defined by

$$\langle f, g \rangle := \mathbb{E}_{x \sim p} [f(x) g(x)], \quad \|f\|_2^2 = \langle f, f \rangle.$$

## 2.1 Neural networks as functions in $L^2(p)$

A neural network with parameters  $\theta \in \mathbb{R}^N$  represents a time-dependent function  $f_{\theta(t)} \in H$ . Given a target function  $f^* \in H$ , we define the error at time  $t$  as

$$e_t := f^* - f_{\theta(t)}.$$

Throughout this work, we emphasize that no structural assumptions such as fixed features, invariant kernels, or predetermined mode decompositions are imposed: the representation  $f_{\theta(t)}$  is allowed to evolve freely in  $H$ , and all structure in the dynamics arises directly from gradient descent.

## 2.2 Gradient descent induces a linear evolution in function space

For MSE loss,

$$\mathcal{L}(\theta) = \frac{1}{2} \|f^* - f_\theta\|_2^2 = \frac{1}{2} \|e\|_2^2,$$

the gradient flow in parameter space is

$$\dot{\theta}(t) = -\nabla_\theta \mathcal{L}(\theta(t)).$$

By the chain rule,

$$\dot{e}_t = -J_{\theta(t)} \dot{\theta}(t),$$

where  $J_\theta: \mathbb{R}^N \rightarrow H$  denotes the Jacobian operator  $(J_\theta v)(x) = \nabla_\theta f_\theta(x) \cdot v$ .

Substituting the gradient flow equation gives

$$\dot{e}_t = -J_{\theta(t)} J_{\theta(t)}^* e_t.$$

Thus the error evolves according to a *linear* operator in function space:

$$\boxed{\dot{e}_t = -M(t) e_t, \quad M(t) := J_{\theta(t)} J_{\theta(t)}^*}.$$

The operator  $M(t)$  is self-adjoint and positive semidefinite. It is the *only* operator that governs the evolution of the error in our analysis; its time dependence reflects the evolving representation of the network under gradient descent.

In this section we work in the continuous-time gradient flow limit,

$$\dot{\theta}(t) = -\nabla_\theta \mathcal{L}(\theta(t)),$$

which corresponds to taking the learning rate to be infinitesimal. A discrete-time update with (possibly time-varying) step sizes  $\eta_k$ ,

$$\theta_{k+1} = \theta_k - \eta_k \nabla_\theta \mathcal{L}(\theta_k),$$

can be viewed as a time reparameterization of this flow, where the effective training time is proportional to the accumulated step size  $\sum_k \eta_k$ . Thus, learning rate schedules do not change the form of the operator dynamics  $\dot{e}_t = -M(t)e_t$ ; instead, they induce a non-uniform rescaling of time that will later be absorbed into the effective time variable  $\tau(t)$  in our spectral analysis.

### 2.3 Spectral decomposition of $M(t)$

For each fixed  $t$ , the operator  $M(t)$  acts on a finite-dimensional subspace of  $H$  determined by the network’s Jacobian, and therefore admits a discrete spectral decomposition. We write

$$M(t) \varphi_u(t) = \lambda_u(t) \varphi_u(t), \quad u \in \mathcal{U}(t),$$

where  $\mathcal{U}(t)$  is a finite or countable index set, the eigenvalues  $\lambda_u(t) \geq 0$ , and the eigenfunctions  $\{\varphi_u(t)\}_{u \in \mathcal{U}(t)}$  form an orthonormal family in  $H$ . Expanding the error in this moving eigenbasis gives

$$e_t = \sum_{u \in \mathcal{U}(t)} g_u(t) \varphi_u(t).$$

The amplitudes  $g_u(t)$  encode how much error lies along each instantaneous mode of  $M(t)$ , and the time dependence of both  $\lambda_u(t)$  and  $\varphi_u(t)$  reflects the evolution of the network’s representation.

### 2.4 Why a spectral formulation?

Although  $M(t)$  generally has low rank compared to the ambient dimension of  $H$ , its eigenstructure provides a natural lens on the error dynamics. The eigenvalues  $\lambda_u(t)$  quantify the rate at which error aligned with mode  $u$  is dissipated, while the evolution of  $\varphi_u(t)$  captures the “feature learning” aspect of training. In Section 3.1, we show that the amplitudes  $g_u(t)$  satisfy a rigorous, coupled system of mode ODEs derived from Kato’s perturbation theory. In Section 3, we then coarse-grain these discrete modes to obtain a continuous spectral PDE that describes the statistical redistribution of error across many nearby modes.

## 3 From Modewise ODEs to Coarse-Grained Spectral Dynamics

In this section we derive the fundamental *coarse-grained spectral structure* governing the dynamics of the error under gradient descent. Starting from the exact

function-space evolution  $\dot{e}_t = -M(t)e_t$ , we first express the dynamics in the instantaneous eigenbasis of  $M(t)$ , obtaining a fully rigorous system of coupled mode-wise ODEs.

Rather than attempting to track individual modes, which is intractable at macroscopic scales, we then introduce a logarithmic spectral-shell coarse-graining and study the evolution of the *quadratic error energy* carried by each shell. This leads to an exact shell-level balance law, in which shell-internal coupling cancels identically and all nontrivial interactions appear as inter-shell energy fluxes.

When the shell spacing is sufficiently fine over a dynamically relevant range, this shell dynamics admits a continuum approximation in the spectral variable  $\lambda$ , yielding a transport–dissipation PDE. However, the shell-level formulation itself is primary and does not rely on any continuum limit. In particular, we never assume that the spectrum becomes continuous or that a limit as the shell spacing vanishes exists; all continuum expressions should be read as local approximations to discrete shell differences.

### 3.1 Exact Mode ODEs in a Drifting Eigenbasis

For each time  $t$ , the operator  $M(t) = J_{\theta(t)}J_{\theta(t)}^*$  is self-adjoint and positive semidefinite, acting on a finite-dimensional subspace of  $H = L^2(p)$ . Thus its spectrum is discrete. Let

$$M(t)\varphi_u(t) = \lambda_u(t)\varphi_u(t), \quad u \in \mathcal{U}(t),$$

denote an orthonormal eigenbasis of  $M(t)$ . Expanding the error in this moving basis gives

$$e_t = \sum_u g_u(t) \varphi_u(t), \quad g_u(t) = \langle e_t, \varphi_u(t) \rangle.$$

Differentiating in time yields

$$\partial_t g_u(t) = \langle \partial_t e_t, \varphi_u(t) \rangle + \langle e_t, \partial_t \varphi_u(t) \rangle.$$

Using  $\dot{e}_t = -M(t)e_t$ , the first term becomes

$$\langle -M(t)e_t, \varphi_u \rangle = -\lambda_u(t)g_u(t).$$

The second term encodes the rotation of the eigenbasis. From Kato’s perturbation theory [Kato, 2012, Zwiebach, 2018] for differential self-adjoint operators, the evolution of the eigenfunctions satisfies

$$\langle \partial_t \varphi_v(t), \varphi_u(t) \rangle = \begin{cases} \frac{\langle \varphi_u(t), \dot{M}(t) \varphi_v(t) \rangle}{\lambda_v(t) - \lambda_u(t)}, & v \neq u, \\ 0, & v = u, \end{cases}$$

where  $\dot{M}(t)$  is the operator derivative of  $M(t)$ . Therefore

$$\langle e_t, \partial_t \varphi_u(t) \rangle = \sum_{v \neq u} g_v(t) \frac{\langle \varphi_u(t), \dot{M}(t) \varphi_v(t) \rangle}{\lambda_v(t) - \lambda_u(t)}.$$

Combining both contributions, we obtain the exact coupled mode ODE:

$$\partial_t g_u(t) + \sum_{v \neq u} g_v(t) \Omega_{v \rightarrow u}(t) = -\lambda_u(t) g_u(t),$$

where the coupling coefficients are

$$\Omega_{v \rightarrow u}(t) = \frac{\langle \varphi_u(t), \dot{M}(t) \varphi_v(t) \rangle}{\lambda_v(t) - \lambda_u(t)}.$$

This ODE system is fully rigorous and contains all aspects of the dynamics: local dissipation  $-\lambda_u g_u$ , nonlocal mode coupling  $\sum_{v \neq u} g_v \Omega_{v \rightarrow u}$ , and the drift of the feature basis through the time dependence of the eigenfunctions  $\varphi_u(t)$ .

### 3.2 Logarithmic Spectral Shells and Shell Energies

The exact modewise dynamics derived in Section 3.1 are fully rigorous but too fine-grained for macroscopic analysis. To expose the coarse structure, we group modes into logarithmic spectral shells and track the *quadratic* error energy carried by each shell.

Fix a ratio  $q > 1$  and define a logarithmic partition of the positive spectrum:

$$\lambda_\alpha := \lambda_0 q^\alpha, \quad S_\alpha := \{ u : \lambda_u(t) \in [\lambda_\alpha, \lambda_{\alpha+1}) \}, \quad \alpha \in \mathbb{Z}.$$

We also define cumulative shells  $S_{\leq \alpha} := \bigcup_{\gamma \leq \alpha} S_\gamma$ .

For each shell, we define the *shell quadratic energy*

$$E_\alpha(t) := \frac{1}{2} \sum_{u \in S_\alpha} g_u(t)^2, \quad E_{\leq \alpha}(t) := \sum_{\gamma \leq \alpha} E_\gamma(t).$$

This choice is canonical: the full function-space loss is  $\mathcal{L}(t) = \frac{1}{2} \|e_t\|_2^2 = \frac{1}{2} \sum_u g_u(t)^2$ , so  $\{E_\alpha\}$  provides an exact energy bookkeeping across spectral shells.

### 3.3 Exact Cancellation of Shell-Internal Coupling for Quadratic Energy

Recall the exact mode ODE

$$\partial_t g_u(t) + \sum_{v \neq u} g_v(t) \Omega_{v \rightarrow u}(t) = -\lambda_u(t) g_u(t), \quad \Omega_{v \rightarrow u}(t) = \frac{\langle \varphi_u(t), \dot{M}(t) \varphi_v(t) \rangle}{\lambda_v(t) - \lambda_u(t)}.$$

Since  $\dot{M}(t)$  is self-adjoint and the denominator is antisymmetric, we have the strict antisymmetry

$$\Omega_{v \rightarrow u}(t) = -\Omega_{u \rightarrow v}(t), \quad u \neq v.$$

**Proposition 1** (Shell-internal cancellation (quadratic energy)). *For any spectral shell  $S_\alpha$ , the shell-internal coupling does not change the quadratic shell energy:*

$$\sum_{u \in S_\alpha} \sum_{v \in S_\alpha, v \neq u} g_v(t) g_u(t) \Omega_{v \rightarrow u}(t) = 0.$$

*Proof.* Pair terms  $(u, v)$  and  $(v, u)$  inside the double sum. Using  $\Omega_{v \rightarrow u} = -\Omega_{u \rightarrow v}$ , we get

$$g_v g_u \Omega_{v \rightarrow u} + g_u g_v \Omega_{u \rightarrow v} = g_u g_v (\Omega_{v \rightarrow u} + \Omega_{u \rightarrow v}) = 0.$$

Summing over all unordered pairs in  $S_\alpha$  yields the claim.  $\square$

*Remark 1* (Interpretation). Proposition 1 formalizes the key point: *shell-internal coupling is a pure redistribution (rotation) of error among modes within the shell.* It can change the individual  $g_u$ 's, but it cannot change  $\sum_{u \in S_\alpha} g_u^2$ . Therefore, any change of the shell energy  $E_\alpha(t)$  must come from (i) local dissipation and (ii) energy exchange with other shells.

### 3.4 Exact Shell Balance Law for Quadratic Energy

Differentiate  $E_\alpha(t) = \frac{1}{2} \sum_{u \in S_\alpha} g_u^2$ :

$$\frac{d}{dt} E_\alpha(t) = \sum_{u \in S_\alpha} g_u(t) \partial_t g_u(t).$$

Substituting the mode ODE yields

$$\frac{d}{dt} E_\alpha(t) = - \sum_{u \in S_\alpha} \lambda_u(t) g_u(t)^2 - \sum_{u \in S_\alpha} \sum_{v \neq u} g_v(t) g_u(t) \Omega_{v \rightarrow u}(t). \quad (1)$$

Split the coupling sum into  $v \in S_\alpha$  and  $v \notin S_\alpha$ . By Proposition 1, the  $v \in S_\alpha$  contribution cancels. Hence we obtain the exact shell energy balance:

$$\boxed{\frac{d}{dt} E_\alpha(t) = - \sum_{u \in S_\alpha} \lambda_u(t) g_u(t)^2 - \sum_{\beta \neq \alpha} \sum_{\substack{u \in S_\alpha \\ v \in S_\beta}} g_v(t) g_u(t) \Omega_{v \rightarrow u}(t).} \quad (2)$$

The first term is *pure shell dissipation*. The second term is *pure inter-shell exchange*.

### 3.5 Inter-Shell Fluxes and Discrete Conservation Structure

Define the inter-shell quadratic-energy flux from  $S_\beta$  to  $S_\alpha$  by

$$\mathcal{F}_{\beta \rightarrow \alpha}(t) := - \sum_{\substack{u \in S_\alpha \\ v \in S_\beta}} g_v(t) g_u(t) \Omega_{v \rightarrow u}(t).$$

Then equation (2) becomes

$$\boxed{\frac{d}{dt} E_\alpha(t) = - \sum_{u \in S_\alpha} \lambda_u(t) g_u(t)^2 + \sum_{\beta \neq \alpha} \mathcal{F}_{\beta \rightarrow \alpha}(t).} \quad (3)$$

Moreover, antisymmetry implies a strict action–reaction identity:

$$\mathcal{F}_{\beta \rightarrow \alpha}(t) = -\mathcal{F}_{\alpha \rightarrow \beta}(t).$$

Therefore, coupling conserves total quadratic energy across shells:

$$\sum_{\alpha} \sum_{\beta \neq \alpha} \mathcal{F}_{\beta \rightarrow \alpha}(t) = 0,$$

and the only mechanism that decreases  $\sum_{\alpha} E_\alpha(t) = \frac{1}{2} \|e_t\|_2^2$  is the dissipation term  $-\sum_u \lambda_u g_u^2$ .

### 3.6 From Exact Shell Balance to Renormalized Dynamics

The balance law (3) is an exact conservation-type bookkeeping equation across logarithmic shells, requiring no continuum limit and no PDE interpretation. However, the fluxes  $\mathcal{F}_{\beta \rightarrow \alpha}(t)$  remain nonlocal and depend on microscopic details of the evolving operator.

In the remainder of the paper, we do not attempt to characterize  $\mathcal{F}_{\beta \rightarrow \alpha}$  microscopically. Instead, Section 4 introduces a *renormalizable shell-dynamics assumption* that closes the cumulative effect of inter-shell fluxes at the shell level. All subsequent results rely exclusively on this shell-level interface.

We emphasize that all subsequent results in this paper rely exclusively on this shell-level energy balance and the renormalizable flux interface introduced in Section 4. The continuum PDE description is used only as a convenient approximation when shell resolution permits.

## 4 Renormalizable Shell Dynamics and Effective Power-Law Transport

Section 3 provides an exact modewise ODE system and an effective spectral PDE description. In this section we introduce an explicitly *coarse-grained* interface for macroscopic analysis: logarithmic spectral shells, a renormalizable flux bookkeeping condition across shells, and a single effective transport assumption used in the remainder of the paper. We emphasize that this section is not a microscopic characterization of all possible operators  $M(t)$ ; rather, it formulates the minimal coarse-grained structure needed to derive self-similar spectral dynamics and scaling laws.

### 4.1 Log-shell partition and quadratic shell energies

Fix a ratio  $q > 1$  and define a logarithmic partition  $\{\lambda_\alpha\}_{\alpha \in \mathbb{Z}}$  by

$$\lambda_\alpha := \lambda_0 q^\alpha, \quad S_\alpha := \{u : \lambda_u(t) \in [\lambda_\alpha, \lambda_{\alpha+1})\}, \quad S_{\leq \alpha} := \bigcup_{\gamma \leq \alpha} S_\gamma.$$

We work with the *quadratic* shell energies introduced in Section 3.2:

$$E_\alpha(t) := \frac{1}{2} \sum_{u \in S_\alpha} g_u(t)^2, \quad E_{\leq \alpha}(t) := \sum_{\gamma \leq \alpha} E_\gamma(t).$$

This choice is canonical because  $\mathcal{L}(t) = \frac{1}{2} \|e_t\|_2^2 = \sum_\alpha E_\alpha(t)$ .

### 4.2 Exact shell bookkeeping and the role of dissipation

Section 3.4 already established the exact identity

$$\frac{d}{dt} E_\alpha(t) = -D_\alpha(t) + \sum_{\beta \neq \alpha} \mathcal{F}_{\beta \rightarrow \alpha}(t), \quad D_\alpha(t) := \sum_{u \in S_\alpha} \lambda_u(t) g_u(t)^2,$$

where  $\mathcal{F}_{\beta \rightarrow \alpha}(t)$  is the inter-shell quadratic-energy flux and satisfies  $\mathcal{F}_{\beta \rightarrow \alpha}(t) = -\mathcal{F}_{\alpha \rightarrow \beta}(t)$ . In particular, *shell-internal coupling does not change  $E_\alpha$*  and the *only* mechanism that decreases  $\sum_\alpha E_\alpha(t)$  is dissipation  $\sum_\alpha D_\alpha(t)$ .

### 4.3 Definition: renormalizable shell dynamics via cumulative *energy* flux

The notion of renormalizability adopted here follows the standard usage in statistical physics and field theory. Rather than requiring microscopic locality or exact continuum limits, external interaction effects on a resolution shell are integrated out and absorbed into effective inter-shell fluxes, while subleading corrections become irrelevant at coarse scales. This philosophy underlies Wilsonian renormalization group theory [Wilson, 1983, Kadanoff, 1966], shell models of turbulence and energy cascades [Kolmogorov, 1995], and effective hydrodynamic descriptions of nonequilibrium systems [Forster et al., 1977, Spohn, 2012]. Our definition formalizes this principle at the level of spectral-shell energy dynamics.

**Definition 4.1** (Renormalizable spectral-shell dynamics (energy form)). The modewise dynamics are said to be *(weakly) renormalizable* with respect to the log-shell partition if, for sufficiently large  $\alpha$ , the shell energies admit a closed balance of the form

$$\frac{d}{dt} E_\alpha(t) = -D_\alpha(t) + \mathcal{F}_\alpha^{(\text{net})}(t) + \mathcal{R}_\alpha(t),$$

where the coarse-grained interaction contribution admits a net-flux form

$$\mathcal{F}_\alpha^{(\text{net})}(t) = J_{\leq \alpha}(t) - J_{\leq \alpha-1}(t),$$

and the remainder is negligible compared to the leading dissipation:

$$|\mathcal{R}_\alpha(t)| \ll D_\alpha(t) \quad \text{as } \alpha \rightarrow \infty.$$

Here  $J_{\leq \alpha}(t)$  is the cumulative *quadratic-energy* flux across the shell boundary at  $\alpha$ , defined by the exact microscopic inter-shell fluxes as

$$J_{\leq \alpha}(t) := \sum_{\beta > \alpha} \mathcal{F}_{\beta \rightarrow (\leq \alpha)}(t) = \sum_{\beta > \alpha} \sum_{\gamma \leq \alpha} \mathcal{F}_{\beta \rightarrow \gamma}(t).$$

Moreover, the cumulative flux is *integrable at coarse scales* in the sense that for each shell  $\alpha$  there exists  $T_\alpha > 0$  such that for all  $T > T_\alpha$ ,

$$\int_0^T |J_{\leq \alpha}(t)| dt \leq C \int_0^T D_\alpha(t) dt.$$

*Remark 2* (What the cumulative flux represents). Definition 4.1 does not assume microscopic locality of coupling. All shells  $\beta > \alpha$  are included in  $J_{\leq \alpha}$ . Renormalizability asserts only that after coarse-graining the net inter-shell exchange can be summarized by a controlled boundary flux plus a negligible remainder.

*Remark 3* (No direction is assumed). Renormalizability imposes no restriction on the sign or direction of  $J_{\leq \alpha}(t)$ . All later results depend only on the existence of a controlled net-flux representation, not on an *a priori* cascade direction.

#### 4.4 PDE-approximability across shells (energy continuum)

When the shell spacing is sufficiently fine over a resolution range, we may introduce an energy density  $\varepsilon(\lambda, t)$  such that

$$E_\alpha(t) \approx \int_{\lambda_\alpha}^{\lambda_{\alpha+1}} \varepsilon(\lambda, t) d\lambda, \quad J_{\leq \alpha}(t) - J_{\leq \alpha-1}(t) \approx \int_{\lambda_\alpha}^{\lambda_{\alpha+1}} J(\lambda, t) d\lambda,$$

This is a *local* continuum approximation over that range; we do not require a global continuous-spectrum limit. As in nonequilibrium statistical physics Forster et al. [1977], Spohn [2012], we do not assume the existence of an exact continuum limit; rather, renormalizability refers to the existence of a closed effective description after coarse-graining. We stress again that our continuum equations do not assume the existence of a genuine continuous-spectrum limit. Under this approximation we acquire the expression of the total loss function:

$$\mathcal{L}(t) \approx \int_{\lambda_{\min}}^{\lambda_{\max}} \varepsilon(\lambda, t) d\lambda.$$

They represent a local approximation of the discrete shell-flux difference when shells are sufficiently dense over a dynamically relevant resolution range. Formally, this amounts to approximating the discrete net-flux difference  $J_{\leq \alpha}(t) - J_{\leq \alpha-1}(t)$  by a first-order finite-difference representation of  $\partial_\lambda J$  over a dense but finite shell range. This energy continuum yields, to leading order, the energy transport-dissipation equation

$$\partial_t \varepsilon(\lambda, t) + \partial_\lambda J(\lambda, t) = -2\lambda \varepsilon(\lambda, t), \quad (4)$$

on the relevant resolution range. The factor 2 reflects the fact that dissipation in the mode ODE is  $-\lambda_u g_u$ , hence quadratic energy dissipates as  $-\frac{d}{dt} \frac{1}{2} g_u^2 = \lambda_u g_u^2$ .

## 4.5 RMS amplitude notation

For compatibility with earlier GSD/GRSD forms, we also define an RMS amplitude density

$$g(\lambda, t) := \sqrt{2 \varepsilon(\lambda, t)}. \quad (5)$$

Then

$$\mathcal{L}(t) \approx \int_{\lambda_{\min}}^{\lambda_{\max}} \varepsilon(\lambda, t) d\lambda = \int_{\lambda_{\min}}^{\lambda_{\max}} g(\lambda, t)^2 d\lambda,$$

and equation (4) can be viewed as the energy-level backbone behind the GRSD tail forms written in terms of  $g$ .

## 4.6 Unified view of NTK and feature learning through spectral transport

The shell-energy formulation provides a clean unification of lazy (NTK-like) training and feature learning through a single macroscopic quantity: the spectral drift velocity  $v(\lambda, t)$ . Recall the definition

$$J(\lambda, t) = v(\lambda, t) g(\lambda, t),$$

which defines the effective transport velocity  $v(\lambda, t)$  in the coarse-grained description.

**Lazy / NTK regime ( $v \equiv 0$ ).** If the kernel operator is effectively frozen during training ( $\dot{M}(t) \approx 0$ ), then  $v(\lambda, t) \equiv 0$  and no inter-shell transport occurs. The shell dynamics reduce to

$$\frac{d}{dt} E_\alpha(t) = -D_\alpha(t),$$

so each shell decays independently under dissipation. No resolution frontier forms, and the dynamics coincide with classical NTK theory.

**Feature learning regime ( $v \neq 0$ ).** When the representation evolves ( $\dot{M}(t) \neq 0$ ), the drift velocity becomes active and induces inter-shell energy transport. Energy is redistributed across resolutions before being dissipated, producing a moving resolution frontier and the GRSD tail described in Sections 5–6.

Crucially, this redistribution preserves total quadratic energy and does not increase training loss. Its observable consequences depend on how the transported energy aligns with the evaluation distribution (training vs. test).

**Continuum of regimes.** Between these extremes lies a continuum:

- If  $|v(\lambda, t)| \ll \lambda$ , dissipation dominates and training is effectively NTK-like.
- If  $|v(\lambda, t)|$  is comparable to or larger than  $\lambda$  over a resolution range, transport reshapes the spectrum and feature learning emerges.

Thus, lazy training and feature learning are not distinct dynamical theories, but limiting behaviors of the same renormalized shell-energy dynamics.

**Interpretation.** From this perspective, feature learning corresponds to *spectral energy transport induced by representation drift*, while NTK corresponds to the degenerate zero-transport limit. Both are unified within the same operator-theoretic framework.

## 4.7 Summary

The key structural takeaway is:

*Shell-internal coupling is a rotation that preserves quadratic energy within each shell. Any macroscopic evolution of shell energies is fully captured by (i) dissipation and (ii) inter-shell boundary flux.*

All scaling-law consequences in later sections are derived from the renormalized boundary-flux interface (4.1)–(4) in a high-resolution range.

## 5 Scale-Free GRSD Under Power-Law-Compatible Transport

In this section we analyze the effective GRSD regime arising in an intermediate scale-free training window. Empirically, modern deep models exhibit extended intervals  $t_0 < t < T$  during which macroscopic spectral observables evolve as straight lines in log–log coordinates, indicating the absence of intrinsic scales.

Within such a window, the effective spectral transport must itself be approximately scale-free. While the most general scale-free drift takes the form  $v(\lambda, t) = \phi(\lambda/t)$ , requiring *pure power-law temporal scaling* of observables rules out generic  $\phi$  and selects the linear scale-free transport

$$v(\lambda, t) = c_0 \frac{\lambda}{t}, \quad t_0 < t < T, \quad (6)$$

up to subleading corrections. In the remainder of this section we take (6) as an effective model assumption and solve the resulting GRSD dynamics explicitly.

**Why scale-free observables rigidly constrain the drift.** We emphasize that the power-law form

$$v(\lambda, t) = c_0 \frac{\lambda}{t}$$

is not introduced as an arbitrary modeling choice. Rather, it is rigidly selected by the requirement that macroscopic spectral observables remain scale-free over an extended training window.

Empirically, in this regime, shell-resolved quantities such as the spectral energy density, cumulative shell energies, and total loss evolve as straight lines in log–log coordinates over multiple decades of time and resolution. This behavior implies not merely scale invariance at a fixed time, but a joint scale covariance between the spectral coordinate  $\lambda$  and the training time  $t$ .

At the level of the coarse-grained shell dynamics, this covariance severely restricts the admissible form of the effective transport velocity. While the most general scale-free drift compatible with dimensional analysis can be written as  $v(\lambda, t) = \phi(\lambda/t)$ , generic choices of  $\phi$  induce nonlinear reparameterizations of the spectral coordinate and therefore produce curvature in log–log observables. Requiring that these observables remain asymptotically affine in log–log space selects the linear form  $\phi(u) = c_0 u$ , yielding  $v(\lambda, t) = c_0 \lambda/t$  up to subleading corrections.

**On the origin of the scale-free drift form.** The specific choice  $v(\lambda, t) = c_0 \lambda/t$  should not be interpreted as an ad hoc modeling assumption. Under a set of strong but practically natural conditions—such as controlled training trajectories, uniformly bounded gradients, and zero-mean random initialization—the same scale-free drift form can be derived directly from the training dynamics. A concrete derivation under such conditions is given in Zhang [2026]. In the present work, we do not rely on these sufficient conditions and instead take Eq. (5) as a macroscopic consequence of scale-free spectral evolution; the aforementioned derivation serves only to demonstrate that the assumed drift is dynamically realizable rather than postulated.

**Lagrangian spectral coordinates as the renormalized frame.** The emergence of the Lagrangian spectral coordinate  $u$  should not be viewed as a technical device introduced solely to solve the transport equation. Instead, it represents the natural renormalized variable induced by the shell-level flux interface.

At the discrete shell level, renormalizability asserts that the cumulative effect of inter-shell interactions can be summarized by a controlled boundary flux. In the continuum approximation, this structure manifests as a transport term that can be absorbed into a time-dependent reparameterization of the spectral coordinate. The characteristic flow Eq. (5) implements precisely this absorption.

In the co-moving coordinate  $u$ , the dynamics reduce to pure dissipation. All nontrivial macroscopic structure—including scaling laws and apparent emergence—is therefore encoded in how this co-moving frame maps back to stationary spectral coordinates. The simplicity of the resulting evolution is not accidental, but a direct consequence of the renormalizable shell-dynamics assumption.

### 5.1 Characteristic flow and scale-free reparameterization

Starting from the leading-order GRSD equation

$$\partial_t \varepsilon(\lambda, t) + \partial_\lambda(v(\lambda, t)\varepsilon(\lambda, t)) = -2\lambda\varepsilon(\lambda, t), \quad (7)$$

with drift (6), the characteristic curves satisfy

$$\frac{d\lambda}{dt} = c_0 \frac{\lambda}{t}. \quad (8)$$

Integrating yields the exact scale-free flow

$$\lambda(t; u) = u \left( \frac{t}{t_0} \right)^{c_0}, \quad u = \lambda \left( \frac{t}{t_0} \right)^{-c_0}, \quad (9)$$

where  $u$  defines a stationary (Lagrangian) spectral coordinate. This flow is strictly power-law and affine in log-log coordinates.

### 5.2 Energy density along characteristics

Along a characteristic  $\lambda(t; u)$ , the energy density evolves as

$$\frac{d}{dt} \log \varepsilon(\lambda(t), t) = -2\lambda(t). \quad (10)$$

Substituting (9) and integrating gives

$$\varepsilon(u, t) = \varepsilon_0(u) \exp \left[ -\frac{2u}{1+c_0} \left( \left( \frac{t}{t_0} \right)^{1+c_0} - 1 \right) \right], \quad c_0 \neq -1. \quad (11)$$

which is aligned with the spectral evolution conjecture proposed in Zhang [2025]:

$$f^* - f_\lambda(t) = w_\lambda \exp(g(\lambda, t)) \quad (12)$$

where  $g(\lambda, t) \propto \lambda^{a(\beta)} t^{b(\beta)}$  and thus  $w_\lambda^2$  correspond to the starting error on mode with eigenvalue of  $\lambda$ . This conjecture is helpful for understanding the scaling law for both loss evolution and model compression. It further predicted the existence of

learning frontier and defines model density, which is observed to evolve according to Xiao et al. [2025].

Rewriting (11) in Eulerian coordinates using  $u = \lambda(t/t_0)^{-c_0}$  yields

$$\varepsilon(\lambda, t) = \varepsilon_0(\lambda t^{-c_0}) \exp\left(-\frac{2\lambda}{1+c_0}t\right). \quad (13)$$

The exponential factor represents physical dissipation, while the prefactor encodes pure scale-free transport. The competition between transport and dissipation is governed entirely by the combination  $1 + c_0$ . This expression constitutes the leading-order GRSD solution in the scale-free window.

At the level of logarithmic spectral shells, the high-resolution behavior of the quadratic error energy can be expressed in a factorized form

$$E_\alpha(t) \approx A(\lambda_\alpha t^{-c_0}) \exp(-\kappa(t) \lambda_\alpha), \quad \lambda_\alpha \text{ beyond the resolution frontier,} \quad (14)$$

where  $\lambda_\alpha$  denotes the representative eigenvalue of shell  $\alpha$ ,  $\kappa(t)$  is an effective dissipation scale, and  $A(\lambda, t)$  is a coarse-grained amplitude capturing the combined effects of spectral transport and initialization.

**Remark (Amplitude structure).** The function  $A(\lambda, t)$  is not assumed to take any specific form in general. *Particularly*, when the initial error spectrum is approximately scale-free over a range of resolutions, the amplitude may inherit a corresponding power-law dependence on  $\lambda$ :

$$\varepsilon(\lambda, t) = (\lambda t^{-c_0})^p \exp\left(-\frac{2\lambda}{1+c_0}t\right) = t^{-c_0 p} (\lambda)^p \exp\left(-\frac{2\lambda}{1+c_0}t\right). \quad (15)$$

which leads to a shell-energy profile of the representative form

$$E_\alpha(t) \sim C(t) \lambda_\alpha^{p+1} \exp(-\kappa(t) \lambda_\alpha), \quad \lambda_\alpha \text{ beyond the frontier,} \quad (16)$$

for some exponent  $p$ . We emphasize that this expression is provided only as an illustrative example of how scale-free initialization can manifest at the shell level; no assumption on the sign or universality of  $p$  is made, and our empirical analysis does not rely on this specific functional form.

The total quadratic loss is

$$\mathcal{L}(t) = \int_{\lambda_{\min}}^{\lambda_{\max}} \varepsilon(\lambda, t) d\lambda \approx \int_{\lambda_{\min}}^{\infty} \varepsilon(\lambda, t) d\lambda. \quad (17)$$

where the approximation holds for an exponential decay as lambda increases. Starting from

$$\varepsilon(\lambda, t) = (\lambda t^{-c_0})^p \exp\left(-\frac{2\lambda}{1+c_0} t\right) = t^{-c_0 p} \lambda^p e^{-at\lambda}, \quad a := \frac{2}{1+c_0}, \quad (18)$$

the total quadratic error is

$$L(t) \approx \int_{\lambda_{\min}}^{\infty} \varepsilon(\lambda, t) d\lambda = t^{-c_0 p} \int_{\lambda_{\min}}^{\infty} \lambda^p e^{-at\lambda} d\lambda. \quad (19)$$

Performing the change of variables  $u = at\lambda$ , we obtain

$$L(t) = t^{-c_0 p} (at)^{-(p+1)} \int_{at\lambda_{\min}}^{\infty} u^p e^{-u} du = t^{-c_0 p} (at)^{-(p+1)} \Gamma(1+p, at\lambda_{\min}). \quad (20)$$

In our theoretic analysis, the time  $t \in (t_0, T)$  is in the scale-free range. For any  $T$  such that  $T\lambda_{\min} \ll \frac{1}{a}$ , the remaining integral converges to a constant as  $t$  varies, yielding the asymptotic scaling

$$L(t) \propto t^{-c_0 p} t^{-(p+1)} = t^{-[(1+c_0)p+1]}. \quad (21)$$

**Transport–dissipation competition and spectral front formation.** The explicit solution reveals a universal structural feature: the dynamics are governed by a competition between scale-free transport and scale-dependent dissipation. Transport alone redistributes error mass across resolutions without loss, while dissipation selectively suppresses high- $\lambda$  components.

Their interplay generates a moving spectral front separating a learned region from an unresolved tail. Importantly, this front is not an artifact of a particular initialization, architecture, or optimizer choice. It is a robust consequence of renormalizable spectral transport under power-law-compatible drift.

In the next section, we show that when training and evaluation are performed on finite samples drawn from the same underlying distribution, this moving front interacts with unavoidable high-resolution spectral mismatch. The resulting transient amplification in certain spectral bands provides a natural and entirely in-domain explanation of the double-descent phenomenon.

## 6 Double Descent from In-Domain Finite-Sample Spectral Mismatch

We now explain the origin of the double-descent phenomenon from the perspective of renormalizable spectral-shell dynamics. Crucially, the mechanism described

here is entirely *in-domain*: training and test data are drawn independently from the same underlying data-generating distribution. The non-monotonicity of the test loss arises not from distribution shift, but from unavoidable finite-sample spectral mismatch concentrated in high-resolution modes.

### 6.1 Training dynamics and monotone training loss.

Throughout training, the error evolves according to

$$\dot{e}_t = -M(t)e_t, \quad M(t) = J_{\theta(t)}J_{\theta(t)}^* \succeq 0.$$

Measured in the training metric, the quadratic loss

$$\mathcal{L}_{\text{tr}}(t) := \frac{1}{2}\|e_t\|_{L^2(p)}^2 = \sum_{\alpha} E_{\alpha}(t), \quad E_{\alpha}(t) := \frac{1}{2} \sum_{u \in S_{\alpha}} g_u(t)^2,$$

is strictly non-increasing:

$$\frac{d}{dt} \mathcal{L}_{\text{tr}}(t) = -\langle e_t, M(t)e_t \rangle \leq 0.$$

This monotonicity is exact and does not rely on any coarse-graining, continuum approximation, or weak-coupling assumption.

### 6.2 In-domain train/test mismatch as a finite-sample effect.

Let  $P_{\text{tr}}$  and  $P_{\text{te}}$  denote the empirical quadratic forms induced by the training and test samples, respectively. Both are unbiased estimators of the same population operator associated with the underlying distribution, but differ due to finite sampling. Define the mismatch operator

$$\Delta := P_{\text{te}} - P_{\text{tr}}.$$

The test loss can be written as

$$\mathcal{L}_{\text{te}}(t) = \frac{1}{2}\langle e_t, P_{\text{te}}e_t \rangle = \mathcal{L}_{\text{tr}}(t) + \frac{1}{2}\langle e_t, \Delta e_t \rangle.$$

The second term captures purely finite-sample effects and vanishes only in the infinite-data limit.

For continuous data distributions or infinite-rank kernel operators, the population spectrum exhibits vanishing eigenvalue gaps in the spectral tail. Classical results on empirical covariance and integral operators show that, in this regime, the associated empirical eigenspaces exhibit  $O(1)$  fluctuations under finite sampling [Koltchinskii and Lounici, 2017, Rosasco et al., 2010]. Consequently, even under in-domain sampling,  $\Delta$  is generically supported on high-resolution (spectral-tail) components and is not co-diagonalizable with the training-induced operator  $M(t)$ .

**Double descent as a generic finite-sample effect.** We stress that the non-monotonic behavior described here does not rely on distribution shift, adversarial sampling, or overparameterization *per se*. It arises generically whenever the population operator exhibits a slowly decaying spectral tail and learning proceeds through a transport-dominated regime.

From this perspective, double descent is not a pathological deviation from monotone learning, but a predictable finite-sample manifestation of renormalizable spectral transport. As model capacity or dataset size increases, the location of the mismatch-dominated spectral region shifts, modifying the timing and magnitude of the transient amplification without eliminating the underlying mechanism.

### 6.3 Transport-induced amplitude reweighting

Starting from the GRSD solution (13), the spectral error density admits the exact factorization

$$\varepsilon(\lambda, t) = A(\lambda, t) \exp\left(-\frac{2\lambda}{1+c_0} t\right), \quad A(\lambda, t) := \varepsilon_0(\lambda t^{-c_0}). \quad (22)$$

The exponential factor represents pure dissipation and is strictly decreasing in time. All non-monotonic behavior at fixed  $\lambda$  is therefore encoded in the amplitude function  $A(\lambda, t)$ , which arises solely from scale-free transport.

**Intuitive picture.** Intuitively, scale-free transport continuously transfers error mass from higher- $\lambda$  modes, which are learned and dissipated rapidly, toward lower- $\lambda$  modes. As a result, even as high-resolution errors decay, part of this error is temporarily deposited onto lower-resolution components, raising their spectral error density.

At the same time, dissipation at scale  $\lambda$  is proportional to  $\lambda \varepsilon(\lambda, t)$ , and is therefore weaker at small  $\lambda$ . The mismatch between fast transport from high  $\lambda$  and delayed dissipation at low  $\lambda$  naturally produces a transient amplification before eventual decay.

Differentiating the amplitude function at fixed  $\lambda$  yields

$$\partial_t A(\lambda, t) = -c_0 \lambda t^{-c_0-1} \varepsilon'_0(\lambda t^{-c_0}). \quad (23)$$

Hence, whenever the initial spectrum is decreasing,  $\varepsilon'_0(u) < 0$ , and  $c_0 > 0$ , the amplitude grows in time:

$$\partial_t A(\lambda, t) > 0.$$

Consequently, the spectral error density  $\varepsilon(\lambda, t)$  can increase transiently at fixed  $\lambda$ , despite overall dissipation and monotone decay of the training loss.

## 6.4 Double descent from transport-induced amplification in the mismatch window

We now formalize how transport-induced amplitude growth leads to double descent when combined with finite-sample spectral mismatch. The key point is that, although the training loss is strictly monotone, the test loss probes a different quadratic form that selectively weights high-resolution spectral components.

**Spectral localization of finite-sample mismatch.** Recall that the test loss can be written as

$$L_{\text{te}}(t) = L_{\text{tr}}(t) + \frac{1}{2} \langle e_t, \Delta e_t \rangle, \quad \Delta := P_{\text{te}} - P_{\text{tr}},$$

where  $\Delta$  is the mismatch operator. Classical results on empirical covariance and integral operators imply that, for continuous data distributions and infinite-rank population operators,  $\Delta$  is generically supported on high-resolution modes, corresponding to small eigenvalues  $\lambda$  of the population operator.

At the coarse-grained level, this implies that there exists a resolution interval

$$\lambda \in [\lambda_-, \lambda_+],$$

which we refer to as the *mismatch window*, such that the dominant contribution to  $\langle e_t, \Delta e_t \rangle$  comes from spectral components in this range. Outside this window, either the modes are well-aligned between train and test or their contribution is suppressed by dissipation.

**Mismatch-weighted test loss and non-monotonicity.** The mismatch contribution to the test loss can be approximated, to leading order, by restricting to the mismatch window:

$$\langle e_t, \Delta e_t \rangle \approx \int_{\lambda_-}^{\lambda_+} w(\lambda) \varepsilon(\lambda, t) d\lambda,$$

where  $w(\lambda) \geq 0$  denotes the coarse-grained spectral weight induced by the finite-sample mismatch operator  $\Delta = P_{\text{te}} - P_{\text{tr}}$  in the instantaneous spectral basis of  $M(t)$ , so that  $w(\lambda) d\lambda$  represents the leading-order contribution of modes with eigenvalues in  $[\lambda, \lambda+d\lambda]$  to the quadratic form  $\langle e_t, \Delta e_t \rangle$ . Formally,  $w(\lambda)$  is defined by coarse-graining the diagonal spectral density of the mismatch operator  $\Delta$  in the instantaneous eigenbasis of  $M(t)$ , i.e.

$$w(\lambda) := \sum_{u: \lambda_u(t) \in [\lambda, \lambda+d\lambda]} \langle \phi_u(t), \Delta \phi_u(t) \rangle / d\lambda,$$

so that  $\langle e_t, \Delta e_t \rangle \approx \int w(\lambda) \varepsilon(\lambda, t) d\lambda$  to leading order.

Substituting the factorized form of  $\varepsilon$  gives

$$\int_{\lambda_-}^{\lambda_+} w(\lambda) A(\lambda, t) \exp\left(-\frac{2\lambda}{1+c_0} t\right) d\lambda.$$

If the mismatch window  $[\lambda_-, \lambda_+]$  intersects the region of spectral coordinates for which  $\partial_t A(\lambda, t) > 0$ , then the integrand exhibits a competition between transport-induced amplification and dissipation. At early times, the growth of  $A(\lambda, t)$  dominates, leading to an increase of the mismatch contribution. At later times, exponential dissipation takes over, forcing eventual decay.

**Sufficient condition for double descent.** We therefore obtain the following sufficient condition: if there exists a time interval and a non-negligible spectral region

$$\lambda \in [\lambda_-, \lambda_+] \quad \text{such that} \quad \partial_t A(\lambda, t) > 0,$$

then the test loss  $L_{\text{te}}(t)$  is necessarily non-monotone, even though the training loss  $L_{\text{tr}}(t)$  decreases monotonically. This non-monotonicity manifests as the classical double-descent curve.

Importantly, this mechanism is entirely in-domain. It does not rely on distribution shift or adversarial effects, but follows generically from the interaction between renormalizable spectral transport and finite-sample spectral mismatch.

## 7 Empirical Spectral-Shell Analysis of LLM Training

This section empirically examines whether the coarse-grained spectral-shell structures assumed by the GRSD framework are observable in realistic large language model (LLM) training checkpoints. Our goal is not to infer microscopic transport mechanisms or fit scaling exponents, but to validate the existence of the shell-level structures required by the theory.

### 7.1 Experimental setup and error definition

**Models and checkpoints.** We analyze publicly released checkpoints from the Pythia model family, including models with 70M, 410M, and 7B parameters. Following the standard Pythia release protocol, checkpoints are provided at regular intervals of approximately 1k optimization steps. All checkpoints analyzed in this section are taken directly from the official releases; no selection based on loss values or convergence criteria is performed.

**Error observable.** Let  $q_\theta(y \mid x)$  denote the model-predicted conditional distribution. Throughout this section, the error signal is defined as the negative log-probability of the ground-truth token,

$$e(x) := -\log q_\theta(y^* \mid x), \quad (24)$$

and all spectral quantities are computed from the squared error  $e(x)^2$ .

**Justification via quadratic approximation of KL.** For language modeling with one-hot (or near one-hot) supervision, the ground-truth conditional distribution satisfies  $p(y^* \mid x) \approx 1$ . In this setting, the KL divergence reduces to the negative log-likelihood,

$$\text{KL}(p\|q_\theta) = -\log q_\theta(y^* \mid x) + \text{const.} \quad (25)$$

Moreover, when  $q_\theta(y^* \mid x) \approx 1$ , a second-order expansion yields the local quadratic approximation

$$\text{KL}(p\|q_\theta) \approx \frac{1}{2} (-\log q_\theta(y^* \mid x))^2. \quad (26)$$

Accordingly, the squared log-probability provides a locally equivalent quadratic error measure, consistent with the mean-squared-error framework underlying the spectral-shell analysis. A more detailed derivation is provided in Appendix A.

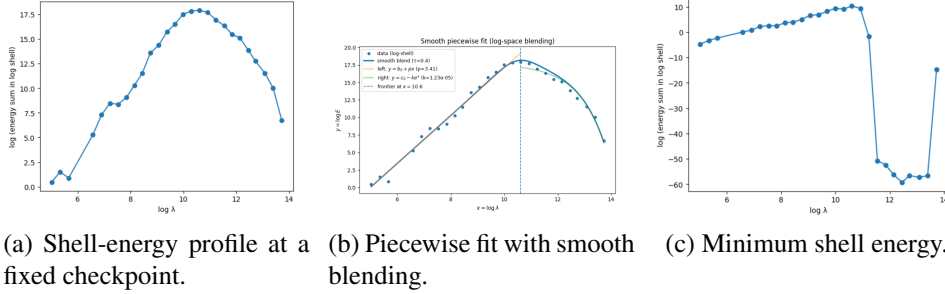
## 7.2 Spectral estimation via stochastic Lanczos

**Motivation.** The operator  $M = J_\theta J_\theta^*$  governing error dynamics acts on a high-dimensional function space, making explicit eigendecomposition infeasible for modern LLMs. To estimate shell-resolved spectral quantities at scale, we employ a stochastic Lanczos method, which probes the spectrum of  $M$  using operator–vector products without explicitly forming  $M$ .

**Shell-energy estimation.** The Lanczos procedure produces a low-dimensional tridiagonal approximation whose spectral measure approximates the projection of the error onto the eigenmodes of  $M$ . The resulting spectral weights are aggregated into logarithmic bins in the spectral coordinate  $\lambda$ , yielding the log-shell–integrated quadratic error energies

$$E_\alpha = \sum_{u: \lambda_u \in [\lambda_\alpha, \lambda_{\alpha+1})} g_u^2, \quad (27)$$

which serve as the primary observables throughout this section. All reported curves correspond to  $\log E_\alpha$  plotted against the shell centers  $\log \lambda_\alpha$ .



(a) Shell-energy profile at a fixed checkpoint. (b) Piecewise fit with smooth blending. (c) Minimum shell energy.

Figure 1: Spectral-shell structure of log-probability error for the 7B Pythia model at a representative checkpoint. **(a)** Minimum energy within each log shell exhibits an abrupt collapse beyond a finite resolution, indicating a sharp dissipation-dominated cutoff rather than an extended power-law tail. **(b)** A piecewise model—log-linear (power-law) behavior on the low-resolution side and exponential suppression beyond the spectral frontier—provides a good qualitative description of the observed profile. The two regimes are combined via a smooth log-space blending for visualization. **(c)** The full log-shell energy distribution forms a robust unimodal profile, with a well-defined spectral frontier separating transport-dominated and dissipation-dominated regimes.

**Data-induced averaging.** To obtain stable shell-level estimates, all spectral quantities are averaged over multiple independent data batches. Specifically, each estimate aggregates results from approximately 50 batches, each consisting of 128 context windows with batch size 4, corresponding to roughly  $2.5 \times 10^5$  tokens in total. No additional stochasticity is introduced in the Lanczos procedure itself; all averaging arises from the data distribution.

Implementation details and pseudocode for the Lanczos-based shell-energy estimation are provided in Appendix B.

### 7.3 Shell-energy structure at a fixed checkpoint

**Theoretical expectation.** As derived in Eq 16, the shell-integrated quadratic error energy admits a factorized form beyond a finite resolution frontier,

$$E_\alpha(t) \approx A(\lambda_\alpha, t) \exp(-\kappa(t) \lambda_\alpha), \quad \lambda_\alpha \text{ beyond the frontier,} \quad (28)$$

where  $A(\lambda, t)$  is a coarse-grained amplitude inherited from transport and initial conditions. In particular, when the initial error spectrum is approximately scale-free over a range of resolutions, the amplitude  $A(\lambda, t)$  may exhibit an effective power-law dependence on  $\lambda$  over that range.

These observations imply the existence of a well-defined *resolution frontier* separating two qualitatively distinct regimes. On the low- $\lambda$  side of the frontier, the shell-integrated error energy varies smoothly across logarithmic shells and is well approximated by an affine trend in log–log coordinates, indicating a slowly varying, transport-dominated structure. As  $\lambda$  increases, the energy profile reaches a single pronounced maximum, beyond which the behavior changes abruptly.

At fixed training checkpoints, the log-shell energy  $E_\alpha$  consistently exhibits a unimodal distribution across resolutions: energy accumulates gradually from low  $\lambda$ , peaks at an intermediate scale, and then decays rapidly at higher resolutions. To probe the high-resolution regime more directly, we examine the minimum error energy within each log shell. Beyond a finite resolution threshold, the minimum shell energy collapses sharply to a numerical floor, producing a clear cutoff on the right side of the spectrum. This abrupt suppression is incompatible with any extended power-law tail and instead indicates a dissipation-dominated regime past the spectral frontier.

#### 7.4 Comparison across checkpoints: spectral-front displacement

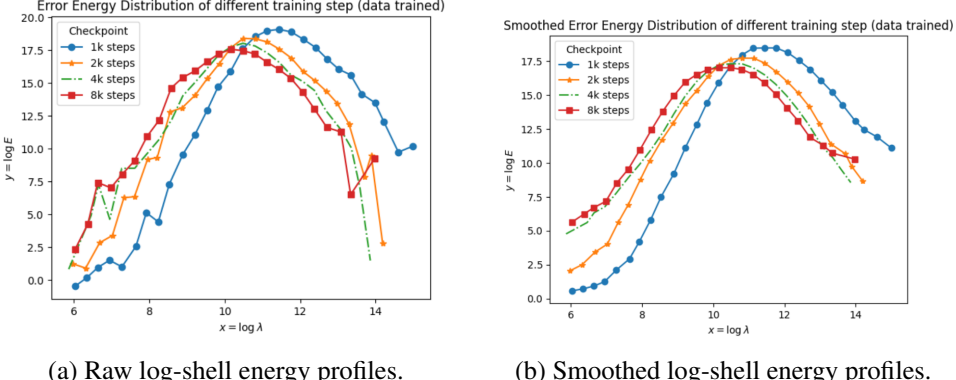
We next compare log-shell energy profiles across multiple training checkpoints for a fixed model. As shown in Fig. 2, the shell-energy distributions at different checkpoints all retain a pronounced unimodal shape, indicating a stable coarse-grained spectral organization throughout training. However, the location of the peak and the extent of the high-resolution tail shift systematically across checkpoints.

In particular, as training progresses, the position of the spectral peak moves toward smaller  $\lambda$ , and the high-resolution side of the distribution contracts accordingly. This behavior is more clearly revealed in the smoothed profiles, which suppress shell-level noise while preserving the global shape. The observed shift reflects a gradual displacement of the effective resolution frontier rather than the emergence of qualitatively new spectral features.

At the same time, the low- $\lambda$  side of the spectrum exhibits coherent reweighting across checkpoints. Over a broad range of low resolutions, the shell-energy curves remain approximately parallel in log–log coordinates, while their overall amplitudes increase with training. This indicates that error energy is redistributed across spectral shells in a correlated manner, rather than decaying independently at fixed resolutions.

#### 7.5 Cross-model consistency across scales

We finally compare shell-energy profiles across models of different scales. Fig. 3 shows the log-shell error energy distributions for Pythia models with 70M and



(a) Raw log-shell energy profiles.

(b) Smoothed log-shell energy profiles.

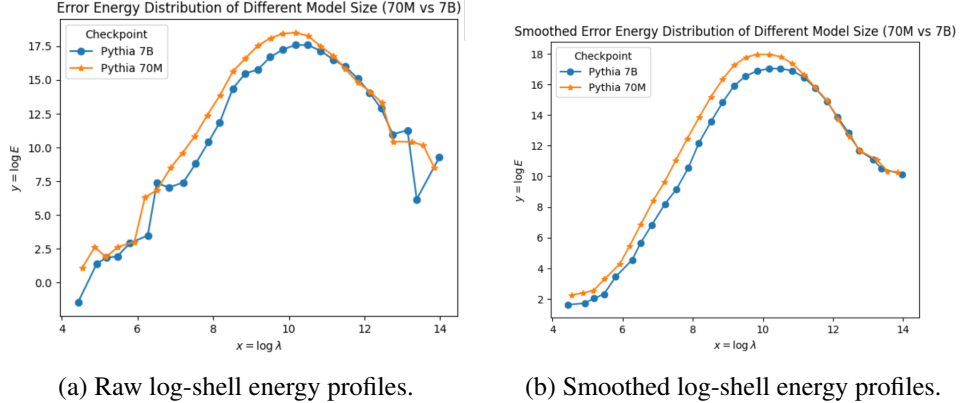
Figure 2: Comparison of log-shell error energy distributions across training checkpoints (1k, 2k, 4k, and 8k steps) for a fixed model. **(a)** Raw shell-energy profiles exhibit a consistent unimodal shape, while the location of the spectral peak and the extent of the high-resolution tail vary systematically across checkpoints. **(b)** Smoothed profiles suppress shell-level fluctuations and more clearly reveal a leftward displacement of the spectral peak and a contraction of the high-resolution tail as training progresses. Across checkpoints, the low- $\lambda$  side of the spectrum remains approximately parallel in log–log coordinates, indicating coherent reweighting of shell energies rather than independent decay at fixed resolutions.

7B parameters at the same checkpoint index. Despite the substantial difference in model size, the two profiles exhibit strikingly similar coarse-grained structure.

In both cases, the shell-energy distribution forms a pronounced unimodal shape, with energy rising smoothly from low  $\lambda$ , peaking at an intermediate resolution, and decaying at higher resolutions. The smoothed profiles further highlight this similarity: across a broad range of resolutions, the two curves closely track each other, differing primarily by an overall amplitude shift and a modest displacement of the peak location.

Notably, the low- $\lambda$  side of the spectrum remains approximately parallel in log–log coordinates across model scales, indicating that the relative distribution of error energy across coarse spectral shells is largely preserved. Differences between the 70M and 7B models manifest mainly in the overall scale of energy and the precise position of the spectral peak, rather than in the emergence of qualitatively new spectral features.

This cross-model consistency suggests that the observed shell-level organization reflects a scale-robust property of training dynamics, rather than an artifact of a particular model size.



(a) Raw log-shell energy profiles. (b) Smoothed log-shell energy profiles.

Figure 3: Cross-model comparison of log-shell error energy distributions for Pythia models with 70M and 7B parameters at the same checkpoint index. **(a)** Raw shell-energy profiles show that both models exhibit a similar unimodal structure, with energy rising from low  $\lambda$ , peaking at an intermediate resolution, and decaying at higher resolutions. **(b)** Smoothed profiles suppress shell-level fluctuations and highlight the close alignment of the two distributions across a broad range of resolutions. Differences between model scales appear primarily as overall amplitude shifts and modest displacements of the spectral peak, while the low- $\lambda$  side of the spectrum remains approximately parallel in log-log coordinates.

## 7.6 Summary of empirical observations

In summary, our experiments establish the following empirical facts: (i) squared log-probability error admits a unimodal shell-energy profile at fixed checkpoints; (ii) a sharp high-resolution frontier exists beyond which shell energy is rapidly suppressed; (iii) the frontier position and low-resolution amplitudes vary coherently across checkpoints; and (iv) these shell-level structures persist across model scales from 70M to 7B parameters.

These observations support the structural assumptions underlying renormalizable spectral-shell dynamics without relying on any specific microscopic transport model.

## 8 Related Work

**Neural scaling laws.** Empirical studies have established that neural networks display remarkably regular power-law relationships between compute, model size, dataset size, and achievable loss [Kaplan et al., 2020, Henighan et al., 2020, Hest-

ness et al., 2017, Hoffmann et al., 2022, Hernandez et al., 2021]. Recent work has investigated both the emergence of such scaling behavior and its theoretical underpinnings, including dynamical models of loss evolution [Bordelon et al., 2024] and the role of data pruning [Sorscher et al., 2022]. Precision scaling laws have also been explored in the context of architectural and quantization constraints [Kumar et al., 2024].

**Feature learning and spectral bias.** A major line of work studies how neural networks acquire hierarchical representations and exhibit spectral preference [Rahaman et al., 2019, Bordelon and Pehlevan, 2024]. Kernel-based analyses of learning dynamics [Bietti and Bach, 2021, Canatar and Pehlevan, 2022] and infinite-width approximations [Jacot et al., 2018a, Lee et al., 2019a, Yang, 2021] have contributed significantly to understanding the transition between lazy training and representation learning. Recent studies have also revealed consistency of learned features across widths [Vyas et al., 2023] and the spectral evolution of networks [Wang et al., 2023].

**Optimization dynamics and stability.** The geometry of optimization landscapes, the effect of batch size, and training stability have been examined extensively [Keskar et al., 2017, Ghorbani et al., 2019]. Work on pruning and compression [Rosenfeld et al., 2021, Han et al., 2016a, Blalock et al., 2020, LeCun et al., 1990, Molchanov et al., 2017, Lee et al., 2019b, Wang et al., 2020, Han et al., 2016b, Nagel et al., 2021, Frantar et al., 2022, Dettmers et al., 2022] has illuminated how spectral structure interacts with parameter sparsity and low-precision computation. Theoretical connections between spectral evolution, implicit bias, and neural dynamics continue to be an active area of research [Dominé et al., 2024, Zhang, 2025].

**Perturbation theory and adiabatic analysis.** Our spectral formulation draws on classical operator perturbation theory [Kato, 2012] and its analogues in quantum adiabatic evolution [Zwiebach, 2018]. These tools formalize how eigenfunctions and eigenvalues evolve under smooth or weakly coupled updates, providing a principled foundation for the drift–dissipation dynamics developed in this work.

## 9 Conclusion

This work proposed a spectral–shell framework for understanding neural scaling laws, feature learning, and double-descent phenomena directly from the operator-level dynamics induced by gradient descent. Starting from the exact function-

space evolution  $\dot{e}_t = -M(t)e_t$ , we derived a rigorous modewise formulation and showed that, upon logarithmic coarse-graining, shell-internal interactions cancel identically at the level of quadratic error energy. As a result, the macroscopic evolution of error is governed entirely by dissipation and inter-shell energy exchange.

The central modeling ingredient of this paper is a *renormalizable spectral-shell dynamics* assumption: after coarse-graining, the cumulative effect of microscopic interactions can be summarized by a controlled net energy flux across shell boundaries. Under an effective power-law form of this renormalized shell-level flux, the shell dynamics admit a self-similar high-resolution tail with a moving resolution frontier. This structure yields explicit scaling-law behavior for the total loss and provides a unified explanation of neural scaling laws and double descent.

A key conceptual outcome of this framework is a unified view of lazy (NTK-like) training and feature learning. When inter-shell transport is negligible, shell energies decay independently under dissipation, recovering classical kernel dynamics. When transport is active, spectral energy is redistributed across resolutions before being dissipated, inducing representation learning. Both regimes—and the continuum between them—are governed by the same shell-energy bookkeeping, differing only in the effective shell-flux interface.

Importantly, the analysis does not assume the existence of a continuous spectrum or a vanishing shell spacing. All continuum partial differential equations appearing in the paper serve only as convenient local approximations of discrete shell-energy dynamics over resolution ranges where shells are sufficiently dense. All scaling-law conclusions can be equivalently interpreted at the discrete shell level.

**Future directions.** Several important questions remain open:

1. **Multi-task and multi-distribution learning.** The present analysis focuses on a single task and a single data distribution. Extending spectral-shell dynamics to multi-task settings—where different task operators may not share eigenbases and may interact through shared representation drift—could reveal new mechanisms of transfer, interference, and modular generalization.
2. **Origin of renormalizability and power-law shell transport.** In this work, the renormalizable shell-flux interface and its effective power-law form are treated as macroscopic assumptions. A natural next step is to understand their qualitative and quantitative origins from operator-level structure. Possible mechanisms include locality of spectral coupling, effective one-directional energy transfer across resolution shells, and the suppression of long-range interactions by stochastic optimization noise. Clarifying when and why such

mechanisms produce renormalizable and power-law shell dynamics would substantially deepen the theoretical foundations of the framework.

3. **Modeling optimizers and learning-rate schedules.** The present formulation is developed for gradient-based optimization with an effective time reparameterization. Momentum, adaptive methods, and second-order or approximate natural-gradient schemes can modify both dissipation and transport. Developing spectral-shell descriptions of these optimizers—and of common learning-rate schedules—may explain optimizer-dependent variations in scaling behavior.
4. **Connecting  $J_\theta$  to network architecture.** The Jacobian operator  $J_\theta$  mediates how parameters generate spectral structure in function space. Understanding how architectural features such as depth, width, and parameterization shape the induced shell dynamics could connect model scaling, representational capacity, and achievable loss within a unified operator-theoretic framework.

Overall, the spectral-shell perspective developed here isolates a minimal and robust macroscopic structure underlying neural training dynamics. By separating exact shell-level conservation laws from coarse-grained flux assumptions, it provides a flexible foundation for understanding scaling phenomena while leaving room for future work on their microscopic origins.

## References

Alberto Bietti and Francis Bach. The inductive bias of neural tangent kernels. *Advances in Neural Information Processing Systems*, 34, 2021.

Davis Blalock, Jose Javier Gonzalez Ortiz, Jonathan Frankle, and John Guttag. What is the state of neural network pruning? *Proceedings of Machine Learning Research*, 2020.

Blake Bordelon and Cengiz Pehlevan. How feature learning can improve neural scaling laws. *arXiv preprint arXiv:2409.17858*, 2024.

Blake Bordelon, Alexander Atanasov, and Cengiz Pehlevan. A dynamical model of neural scaling laws. *arXiv preprint arXiv:2402.01092*, 2024.

Abdulkadir Canatar and Cengiz Pehlevan. A kernel analysis of feature learning in deep neural networks. In *2022 58th Annual Allerton Conference on Communication, Control, and Computing (Allerton)*, pages 1–8. IEEE, 2022.

Tim Dettmers, Mike Lewis, Sam Shleifer, and Luke Zettlemoyer. 8-bit optimizers via block-wise quantization. *Advances in Neural Information Processing Systems*, 2022.

Clémentine CJ Dominé, Nicolas Anguita, Alexandra M Proca, Lukas Braun, Daniel Kunin, Pedro AM Mediano, and Andrew M Saxe. From lazy to rich: Exact learning dynamics in deep linear networks. *arXiv preprint arXiv:2409.14623*, 2024.

Dieter Forster, David R Nelson, and Michael J Stephen. Large-distance and long-time properties of a randomly stirred fluid. *Physical Review A*, 16(2):732, 1977.

Elias Frantar, Saleh Ashkboos, Torsten Hoefer, and Dan Alistarh. Gptq: Accurate post-training quantization for generative pre-trained transformers. *arXiv preprint arXiv:2210.17323*, 2022.

Behrooz Ghorbani, Shankar Krishnan, and Ying Xiao. An investigation into neural net optimization via hessian eigenvalue density. *International Conference on Machine Learning (ICML)*, 2019.

Song Han, Huizi Mao, and William J Dally. Deep compression: Compressing deep neural networks with pruning, trained quantization and huffman coding. In *International Conference on Learning Representations (ICLR)*, 2016a.

Song Han, Huizi Mao, and William J. Dally. Deep compression: Compressing deep neural networks with pruning, trained quantization and huffman coding. In *International Conference on Learning Representations (ICLR)*, 2016b. URL <https://arxiv.org/abs/1510.00149>.

Tom Henighan, Jared Kaplan, Mayank Katz, Mark Chen, Christopher Hesse, Jacob Jackson, Heewoo Jun, Tom Brown, Prafulla Dhariwal, Scott Gray, et al. Scaling laws for autoregressive generative modeling. *arXiv preprint arXiv:2010.14701*, 2020.

Danny Hernandez, Jared Kaplan, Tom Henighan, and Sam McCandlish. Scaling laws and interpretability of learning from diverse data sources. *arXiv preprint arXiv:2109.07437*, 2021.

Joel Hestness, Sharan Narang, Newsha Ardalani, Greg Diamos, Heewoo Jun, Hassan Kianinejad, Mostofa Patwary, Yang You Ali, Yanqi Zhou, and Paulius Micikevicius. Deep learning scaling is predictable, empirically. In *Proceedings of the 2017 Workshop on ML Systems*, 2017.

Jordan Hoffmann, Sebastian Borgeaud, Arthur Mensch, Elena Buchatskaya, Trevor Cai, Eliza Rutherford, Diego de Las Casas, Lisa Anne Hendricks, Johannes Welbl, Aidan Clark, et al. Training compute-optimal large language models. *arXiv preprint arXiv:2203.15556*, 2022.

Arthur Jacot, Franck Gabriel, and Clément Hongler. Neural tangent kernel: Convergence and generalization in neural networks. *Advances in Neural Information Processing Systems*, 31, 2018a.

Arthur Jacot, Franck Gabriel, and Clément Hongler. Neural tangent kernel: Convergence and generalization in neural networks. In *Advances in Neural Information Processing Systems (NeurIPS)*, pages 8571–8580, 2018b. URL <https://arxiv.org/abs/1806.07572>.

Leo P Kadanoff. Scaling laws for ising models near t c. *Physics Physique Fizika*, 2(6):263, 1966.

Jared Kaplan, Sam McCandlish, Tom Henighan, Tom B. Brown, Benjamin Chess, Rewon Child, Scott Gray, Alec Radford, Jeffrey Wu, and Dario Amodei. Scaling laws for neural language models. *arXiv preprint arXiv:2001.08361*, 2020.

Tosio Kato. *A short introduction to perturbation theory for linear operators*. Springer Science & Business Media, 2012.

Nitish Shirish Keskar, Dheevatsa Mudigere, Jorge Nocedal, Mikhail Smelyanskiy, and Ping Tak Peter Tang. On large-batch training for deep learning: Generalization gap and sharp minima. *International Conference on Learning Representations (ICLR)*, 2017.

Andreĭ Nikolaevich Kolmogorov. *Turbulence: the legacy of AN Kolmogorov*. Cambridge university press, 1995.

Vladimir Koltchinskii and Karim Lounici. Normal approximation and concentration of spectral projectors of sample covariance. *The Annals of Statistics*, 45(1): 121–157, 2017.

Tanishq Kumar, Zachary Ankner, Benjamin F Spector, Blake Bordelon, Niklas Muennighoff, Mansheej Paul, Cengiz Pehlevan, Christopher Ré, and Aditi Raghunathan. Scaling laws for precision. *arXiv preprint arXiv:2411.04330*, 2024.

Yann LeCun, John S Denker, and Sara A Solla. Optimal brain damage. In *Advances in Neural Information Processing Systems*, 1990.

Jaehoon Lee, Lechao Xiao, Samuel S Schoenholz, Yasaman Bahri, Roman Novak, Jascha Sohl-Dickstein, and Jeffrey Pennington. Wide neural networks of any depth evolve as linear models under gradient descent. *Advances in Neural Information Processing Systems*, 32, 2019a.

Namhoon Lee, Thalaiyasingam Ajanthan, and Philip H.S. Torr. Snip: Single-shot network pruning based on connection sensitivity. In *International Conference on Learning Representations (ICLR)*, 2019b.

Dmitry Molchanov, Arsenii Ashukha, and Dmitry Vetrov. Variational dropout sparsifies deep neural networks. *Proceedings of the 34th International Conference on Machine Learning*, 2017.

Markus Nagel, Raja Amjad, Mart van Baalen, Tijmen Blankevoort, and Max Welling. Up or down? adaptive rounding for post-training quantization. *International Conference on Machine Learning (ICML)*, 2021.

Nasim Rahaman, Aristide Baratin, Devansh Arpit, Felix Draxler, Min Lin, Fred Hamprecht, Yoshua Bengio, and Aaron Courville. On the spectral bias of neural networks. *Proceedings of Machine Learning Research*, 2019.

Lorenzo Rosasco, Mikhail Belkin, and Ernesto De Vito. On learning with integral operators. In *Advances in Neural Information Processing Systems*, volume 23, pages 1883–1891, 2010.

Jonathan S Rosenfeld, Jonathan Frankle, Michael Carbin, and Nir Shavit. On the predictability of pruning across scales. In *International conference on machine learning*, pages 9075–9083. PMLR, 2021.

Ben Sorscher, Robert Geirhos, Shashank Shekhar, Surya Ganguli, and Ari Mordos. Beyond neural scaling laws: beating power law scaling via data pruning. *Advances in Neural Information Processing Systems*, 35:19523–19536, 2022.

Herbert Spohn. *Large scale dynamics of interacting particles*. Springer Science & Business Media, 2012.

Nikhil Vyas, Alexander Atanasov, Blake Bordelon, Depen Morwani, Sabarish Sainathan, and Cengiz Pehlevan. Feature-learning networks are consistent across widths at realistic scales. *Advances in Neural Information Processing Systems*, 36:1036–1060, 2023.

Alexander Wang, Niranjan Vyas, and Cengiz Pehlevan. Spectral evolution and invariance in linear-width neural networks. In *Advances in Neural Information*

*Processing Systems (NeurIPS)*, 2023. URL <https://arxiv.org/abs/2211.06506>.

Chaoqi Wang, Guodong Zhang, and Roger Grosse. Picking winning tickets before training by preserving gradient flow. In *International Conference on Learning Representations (ICLR)*, 2020.

Jason Wei, Yi Tay, Rishi Bommasani, Colin Raffel, Barret Zoph, Sebastian Borgeaud, Dani Yogatama, Maarten Bosma, Denny Zhou, Donald Metzler, et al. Emergent abilities of large language models. *arXiv preprint arXiv:2206.07682*, 2022.

Kenneth G Wilson. The renormalization group and critical phenomena. *Reviews of Modern Physics*, 55(3):583, 1983.

Chaojun Xiao, Jie Cai, Weilin Zhao, Biyuan Lin, Guoyang Zeng, Jie Zhou, Zhi Zheng, Xu Han, Zhiyuan Liu, and Maosong Sun. Densing law of llms. *Nature Machine Intelligence*, pages 1–11, 2025.

Greg Yang. Tensor programs iv: Feature learning in infinite-width neural networks. In *Proceedings of the 38th International Conference on Machine Learning (ICML)*, 2021. URL <https://arxiv.org/abs/2011.14522>.

Yizhou Zhang. A generalized spectral framework to expain neural scaling and compression dynamics. *arXiv preprint arXiv:2511.07892*, 2025.

Yizhou Zhang. When does learning renormalize? sufficient conditions for power law spectral dynamics, 2026. URL <https://arxiv.org/abs/2512.18209>.

Barton Zwiebach. Mit 8.06 quantum physics iii: Chapter 6 – the adiabatic approximation. <https://ocw.mit.edu>, 2018. See Eq. (3.9).

## A KL-to-MSE justification for log-probability error

This appendix justifies the quadratic error observable used in the empirical spectral-shell analysis. In language modeling with one-hot supervision, the ground-truth conditional distribution is concentrated at the correct token  $y^*$ , while the model predicts  $q_\theta(\cdot | x)$ . For a fixed context  $x$ , the token-level KL divergence satisfies

$$\text{KL}(p(\cdot | x) \| q_\theta(\cdot | x)) = \sum_y p(y | x) \log \frac{p(y | x)}{q_\theta(y | x)} = -\log q_\theta(y^* | x) + C(x),$$

where  $C(x)$  depends only on  $p(\cdot | x)$  and is independent of  $\theta$ .

Define the (log-probability) error observable

$$e(x) := -\log q_\theta(y^* | x).$$

When the model is already assigning high probability to the correct token,  $q_\theta(y^* | x) \approx 1$ , we have  $e(x) \approx 0$  and a local quadratic approximation is appropriate. Consider  $q = \exp(-e)$ , so that  $q \approx 1$  iff  $e \approx 0$ . Expanding  $\exp(-e)$  around  $e = 0$  gives

$$q = e^{-e} = 1 - e + \frac{1}{2}e^2 + O(e^3), \quad \Rightarrow \quad 1 - q = e + O(e^2).$$

Thus, in a neighborhood of  $q = 1$ , any smooth loss functional that is minimized at  $q = 1$  admits a second-order expansion in  $e$ . In particular, the KL divergence above equals  $e$  up to an additive constant, and its *local quadratic surrogate* takes the form

$$\text{KL}(p \| q_\theta) \approx \frac{1}{2} e(x)^2 \quad \text{for } e(x) \ll 1 \ (q_\theta(y^* | x) \approx 1).$$

Therefore, using the squared log-probability  $e(x)^2$  as a mean-squared error observable is consistent with the quadratic-loss framework that underlies the spectral-shell bookkeeping: the induced operator dynamics and shell-energy definitions apply directly once the error signal is taken to be  $e(x)$  and the energy density is built from  $e(x)^2$ .

**Remark (what is measured empirically).** All empirical spectra in this paper are computed from the squared error  $e(x)^2 = (-\log q_\theta(y^* | x))^2$  and then aggregated into logarithmic spectral shells.

## B Spectral estimation via (stochastic) Lanczos and shell binning

This appendix describes the Lanczos-based estimator used to obtain log-shell energies without forming the operator  $M = J_\theta J_\theta^*$  explicitly.

### B.1 Goal: shell energies from the spectral measure of $M$

Fix a checkpoint  $\theta$  and let  $M := J_\theta J_\theta^*$  be the PSD operator governing error dynamics in function space. Let  $e$  denote the error signal (Section ??; in our experiments

$e(x) = -\log q_\theta(y^* \mid x)$ . Formally diagonalizing  $M\phi_u = \lambda_u\phi_u$  and expanding  $e = \sum_u g_u\phi_u$ , the shell-integrated energy is

$$E_\alpha := \sum_{u: \lambda_u \in [\lambda_\alpha, \lambda_{\alpha+1})} g_u^2.$$

Equivalently, define the spectral measure  $\mu_e$  of  $M$  induced by  $e$  so that for any test function  $f$ ,

$$\langle e, f(M)e \rangle = \int f(\lambda) d\mu_e(\lambda), \quad d\mu_e(\lambda) = \sum_u g_u^2 \delta(\lambda - \lambda_u) d\lambda.$$

Then  $E_\alpha$  is exactly the mass of  $\mu_e$  in the bin  $[\lambda_\alpha, \lambda_{\alpha+1})$ .

## B.2 Lanczos tridiagonalization and quadrature

Lanczos constructs, from repeated applications of  $M$  to vectors, an orthonormal basis of the Krylov subspace  $\mathcal{K}_m(M, v_0) = \text{span}\{v_0, Mv_0, \dots, M^{m-1}v_0\}$  and a symmetric tridiagonal matrix  $T_m \in \mathbb{R}^{m \times m}$  such that

$$MV_m \approx V_m T_m, \quad V_m = [v_0, \dots, v_{m-1}], \quad V_m^* V_m = I.$$

We choose the starting vector to be the normalized error direction

$$v_0 := \frac{e}{\|e\|}.$$

Let  $T_m = U \text{diag}(\tilde{\lambda}_i) U^*$  be the eigendecomposition of the tridiagonal matrix. Then Gauss quadrature yields an approximation of the spectral measure  $\mu_e$  by the discrete measure

$$\mu_e(d\lambda) \approx \|e\|^2 \sum_{i=1}^m w_i \delta(\lambda - \tilde{\lambda}_i) d\lambda, \quad w_i := (U_{1i})^2,$$

where  $U_{1i}$  is the first component of the  $i$ -th eigenvector of  $T_m$ .

## B.3 Log-shell binning

Given logarithmic bin edges  $\{\lambda_\alpha\}_{\alpha=0}^B$ , define the estimated shell energies by accumulating quadrature masses:

$$\hat{E}_\alpha := \|e\|^2 \sum_{i: \tilde{\lambda}_i \in [\lambda_\alpha, \lambda_{\alpha+1})} w_i.$$

We report  $\log \hat{E}_\alpha$  as a function of  $\log \lambda_\alpha^{\text{ctr}}$ , where  $\lambda_\alpha^{\text{ctr}}$  is the geometric bin center.

---

**Algorithm 1** Lanczos shell-energy estimation at a fixed checkpoint

---

**Require:** Operator-vector product routine  $u \mapsto Mu$ ; error vector  $e$ ; Lanczos steps

$m$ ; log-shell edges  $\{\lambda_\alpha\}_{\alpha=0}^B$ .

**Ensure:** Estimated shell energies  $\widehat{E}_\alpha$ .

```
1:  $v_0 \leftarrow e/\|e\|$ ;  $\beta_0 \leftarrow 0$ ;  $v_{-1} \leftarrow 0$ 
2: for  $k = 0, \dots, m-1$  do
3:    $w \leftarrow Mv_k - \beta_k v_{k-1}$ 
4:    $\alpha_k \leftarrow \langle v_k, w \rangle$ 
5:    $w \leftarrow w - \alpha_k v_k$ 
6:    $\beta_{k+1} \leftarrow \|w\|$ 
7:   if  $\beta_{k+1} = 0$  then break
8:   end if
9:    $v_{k+1} \leftarrow w/\beta_{k+1}$ 
10:  end for
11:  Form tridiagonal  $T$  with diagonal entries  $\alpha_k$  and off-diagonals  $\beta_{k+1}$ 
12:  Compute eigendecomposition  $T = U \text{diag}(\tilde{\lambda}_i) U^*$ 
13:  Set weights  $w_i \leftarrow (U_{1i})^2$ 
14:  Initialize  $\widehat{E}_\alpha \leftarrow 0$  for all  $\alpha = 0, \dots, B-1$ 
15:  for  $i = 1, \dots, m$  do
16:    Find  $\alpha$  such that  $\tilde{\lambda}_i \in [\lambda_\alpha, \lambda_{\alpha+1})$ 
17:    if such  $\alpha$  exists then
18:       $\widehat{E}_\alpha \leftarrow \widehat{E}_\alpha + \|e\|^2 w_i$ 
19:    end if
20:  end for
21:  return  $\{\widehat{E}_\alpha\}_{\alpha=0}^{B-1}$ 
```

---

#### B.4 Data-induced averaging (no extra randomness)

We do not rely on a global random seed. Variance reduction is achieved by averaging the resulting shell estimates across many independent data batches: each batch provides an empirical error vector  $e$  (computed from a large set of tokens), and the above Lanczos+binning pipeline produces  $\widehat{E}_\alpha$  for that batch; we then average  $\widehat{E}_\alpha$  over batches.

#### B.5 Pseudo-code

**Implementation note.** The only required primitive is the product  $u \mapsto Mu = J_\theta(J_\theta^*u)$ . In modern autodiff frameworks this can be implemented via a VJP followed by a JVP, without constructing  $J_\theta$  or  $M$  explicitly.